Convection and correlation of coherent structure in turbulent boundary layer using tomographic particle image velocimetry

2014 Chinese Phys. B 23 104703

(http://iopscience.iop.org/1674-1056/23/10/104703)

Convection and correlation of coherent structure in turbulent boundary layer using tomographic particle image velocimetry*

Wang Wei(王 维)[a], Guan Xin-Lei(管新蕾)[a], and Jiang Nan(姜 楠)[a)b)c)†]

[a] Department of Mechanics, Tianjin University, Tianjin 300072, China
[b] Tianjin Key Laboratory of Modern Engineering Mechanics, Tianjin 300072, China
[c] The State Key Laboratory of Nonlinear Mechanics, Institute of Mechanics, Chinese Academy of Sciences, Beijing 100190, China

(Received 25 November 2013; revised manuscript received 1 April 2014; published online 20 August 2014)

The present experimental work focuses on a new model for space–time correlation and the scale-dependencies of convection velocity and sweep velocity in turbulent boundary layer over a flat wall. A turbulent boundary layer flow at $Re_\theta = 2460$ is measured by tomographic particle image velocimetry (tomographic PIV). It is demonstrated that arch, cane, and hairpin vortices are dominant in the logarithmic layer. Hairpins and hairpin packets are responsible for the elongated low-momentum zones observed in the instantaneous flow field. The conditionally-averaged coherent structures systemically illustrate the key roles of hairpin vortice in the turbulence dynamic events, such as ejection and sweep events and energy transport. The space–time correlations of instantaneous streamwise fluctuation velocity are calculated and confirm the new elliptic model for the space–time correlation instead of Taylor hypothesis. The convection velocities derived from the space–time correlation and conditionally-averaged method both suggest the scaling with the local mean velocity in the logarithmic layer. Convection velocity result based on Fourier decomposition (FD) shows stronger scale- dependency in the spanwise direction than in streamwise direction. Compared with FD, the proper orthogonal decomposition (POD) has a distinct distribution of convection velocity for the large- and small-scales which are separated in light of their contributions of turbulent kinetic energy.

Keywords: turbulent boundary layer, tomographic particle image velocimetry, space–time correlation, elliptic model

PACS: 47.27.De, 47.27.nb, 47.27.eb, 47.27.ed **DOI:** 10.1088/1674-1056/23/10/104703

1. Introduction

In the past several decades, coherent structure[1] has come out as a breakthrough in the field of turbulence. It brought the organization into turbulence, which had been previously regarded as a pure random fluid motion. Turbulent boundary layer flow over a flat plate with zero pressure gradient is a canonical wall-bounded turbulent flow and composed of a broad range of temporal and spatial scales of coherent structures. The most recognized coherent structure in turbulent boundary layer flow is the low-speed streak in near wall region, which was first observed by Kline *et al.*[2] Subsequent investigations like Brooke and Hanratty,[3] Jeong *et al.*[4] and Schoppa and Hussain[5] confirmed that quasi-streamwise vortices are responsible for the production of these streaks and self-sustaining of turbulence in near wall region. In the outer layer, hairpin vortices are of the dominant coherent structure. The strongest experimental support for the existence of hairpin vortices in the outer layer is given by Head and Bandyopadhyay.[6] In the past three decades, particle image velocimetry (PIV) has had a rapid and explosive development.[7–9] Adrian *et al.*[10] and Tomkins and Adrian[11] summarized the most recognized signatures of hairpin vortices and hairpin packets using PIV. Zhou *et al.*[12] simulated the production process of hairpin packet through a single strong hairpin vortex. Coherent structures distributed in the different layers play a major role in the spatial organization of momentum and energy exchange[13–17] and are connected to the significant dynamic events, such as ejection and sweep events, called Q2 and Q4 events.[18]

The correlation of velocities at two time and two spatial points, i.e. space–time correlation, is a fundamental description of space–time fluctuations in turbulence. However, it is always a huge challenge to simultaneously acquire precise space–time correlation both in the spatial and temporal scales. Researchers hope to find a connection between the space–time correlation and space correlation and further express the space–time correlation in terms of space correlation. The most famous expression is the 'Taylor frozen hypothesis'[19] which assumes that flow structures do not change significantly within certain time limits whiling moving downstream in a turbulent flow. Taylor hypothesis relates the space–time correlation to the space correlation via

$$C(r,\tau) = C(r - U\tau, 0), \tag{1}$$

*Project supported by the National Natural Science Foundation of China (Grant Nos. 11332006 and 11272233) and the National Key Basic Research and Development Program of China (Grant No. 2012CB720101).

†Corresponding author. E-mail: nanj@tju.edu.cn

where C is the correlation coefficient normalized by the root mean square (rms) of the velocity fluctuation, r is the space separation, τ is the time delay, and U is the local longitudinal mean velocity. Taylor hypothesis has other limits such as high turbulence intensity, viscous effect, and the mean shear.[20] In a word, Taylor hypothesis is a crude first-order approximation for the space–time correlation. Turbulent research method such as aeroacoustics, large eddy simulation (LES), etc. are highly dependent on the accuracy of space–time correlation, and will benefit greatly from the advancement of space–time correlation. He and Zhang,[21] Zhao and He,[22] and Guo *et al.*[23] first proposed a new model for the space–time correlation. They related the space–time correlation to the space correlation via

$$C(r,\tau) = C(\sqrt{(r-U_c\tau)^2+(V\tau)^2},0), \tag{2}$$

where U_c is the convection velocity and V is the sweep velocity. Equation (2) indicates that the iso-correlation lines follow the following equation:

$$(r-U_c\tau)^2+(V\tau)^2 = r_E^2, \tag{3}$$

which implies an elliptic shape for every iso-correlation contour. The new model for the space–time correlation is called 'elliptic model'. Besides numerical verification,[21,22] Zhou *et al.*[24] experimentally verified the elliptic model in a turbulent Rayleigh–Bénard convection. As a commonest flow, the validity of the elliptic model in turbulent boundary layer is one of our work's goals.

The convection of coherent structures plays a crucial role in their evolutions because during the convection, they experience topological changes and interactions with each other. In Taylor hypothesis, the convection velocity is assumed to be independent of scale. It is valid only for a few turbulent flows and in most of other turbulent flows, especially wall-bounded turbulence into which the shear brings a variety of scales, the postulate of convection velocity will lead to enormous errors. Kim and Hussain[25] found that the convection velocity presents a spanwise-scale dependency instead of streamwise-scale in a stimulated turbulent channel flow. Krogstad *et al.*[26] experimentally presented similar results that coherent motions of the order of boundary layer thickness convect at the local mean velocity. Del Alamo and Jiménez[27] achieved a more detailed numerical work about scale influence on the convection velocity and proposed a complicated semi-empirical formula. In a novel investigation of convection, Elsinga *et al.*[28] tracked coherent structures one by one in a turbulent boundary layer flow instead of deduction from correlations.

The present work is experimentally accomplished in turbulent boundary layer flow with three-dimensional (3D) tomographic PIV. The first goal of the present work is to verify the elliptic model in the nonhomogeneous flow. The second goal is to investigate the scale-dependency of dominant parameters in the elliptic model, i.e., the convection velocity and the sweep velocity. The scale separation of coherent motions in the flow is implemented through FD and POD from which the distinct behaviors of scales are brought out.

2. Experimental parameters

The experiment was conducted in the water tunnel of the Laboratory for Aero and Hydrodynamics at TU Delft. The turbulent boundary layer data were obtained using tomographic PIV[11,12] and presented by Schröder *et al.*[15] to study the coherent structures in the turbulent boundary layer. The schematic diagram of experiment configuration is shown in Fig. 1. The basic properties of TBL are listed in Table 1. More experimental details can be found in Ref. [15]. The fundamental velocity profile and Reynolds stress profiles were shown in Fig. 2 of their paper, which are not shown here for brevity.

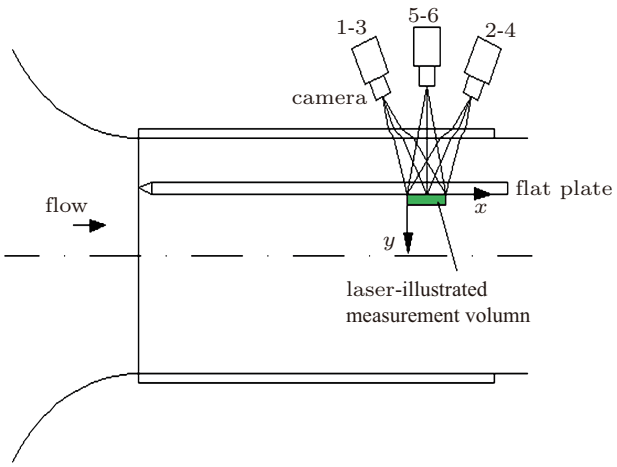

Fig. 1. (color online) Setup of experimental measurement.

Table 1. Basic properties of turbulent boundary layer over a flat wall.

U_e	0.53 m/s
δ	38.1 mm
u_τ	0.022 m/s
Inner length scale (Wall Unit)	
$\frac{\nu}{u_\tau}$	0.0467 mm
$Re_\theta = U_e\theta/\nu$	2460
$Re_\tau = u_\tau\delta/\nu$	800
Increments of vectors in x-, y-, and z directions	0.6872 mm (14.7 WU)

3. Turbulent boundary layer

3.1. Coherent structure in instantaneous flow field

Coherent structure in turbulent boundary layer is generally related to vortical structure which is critical in flow dynamic model for wall-bounded turbulence. In the present work

the vortical structures are distinguished by swirling strength criterion,[11,12,29,30] which suggests that when ∇v has a pair of complex conjugate eigenvalues ($\lambda_{cr} \pm i\lambda_{ci}$), the local flow is a swirling motion and λ_{ci} is a measure of the local swirling rate inside the vortex, i.e., the time period for completing one revolution, $2\pi/\lambda_{ci}$. The detected vortical structures in the flow are shown in Fig. 2(a). All three coordinates are normalized by boundary layer thickness δ, corresponding to the length ranges of 1.32δ, 1.76δ, 0.29δ in streamwise, spanwise, and wall-normal direction respectively. In the plot red surfaces denote the identified vortical structures which have a λ_{ci} value of above 19 while blue surfaces denote the low-speed zones smaller than $0.9U_e$. Symbol 'A' refers to arch vortices, symbol 'C' refers to cane vortices. In the instantaneous turbulent flow field the arch and cane vortices are prevalent in the logarithmic layer, which is consistent with the previous observation.[1,31] Two hairpins in a hairpin packet are specifically marked by symbol 'H1' (upstream) and 'H2' (downstream), and beneath their heads and between their legs are the induced low-speed zones. Hairpin H1 is 0.2δ wide, and inclines 58° with respect to the streamwise direction, while hairpin H2 is 0.4δ wide and inclines 74°. The two hairpins align roughly in the streamwise direction. It is noted that hairpin H2 does not have a perfect symmetric shape. In Zhou *et al.*'s simulation,[12] it is demonstrated that asymmetric hairpins have stronger growth than symmetric hairpins.

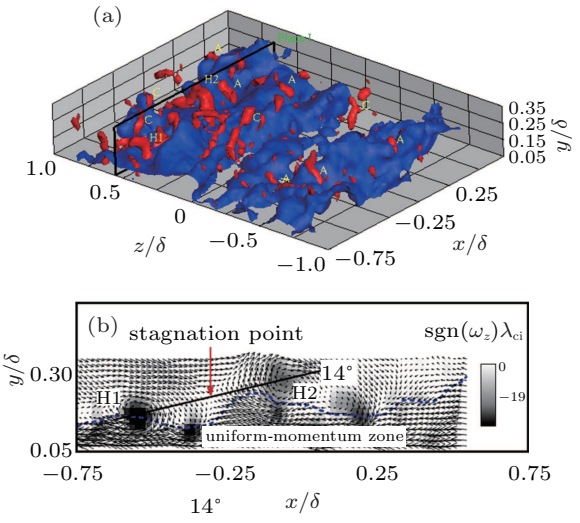

Fig. 2. (color online) (a) Instantaneous 3D turbulent flow field. Red surfaces denote vertical structures identified by λ_{ci} criterion, and the threshold value for visualization is 19. Blue surfaces denote the low speed zones $u < 0.9U_e$ in the flow. The letter 'A' denotes the arch vortices, 'C' represents the cane vortices, 'H1' refers to the lower hairpin in a hairpin packet, and 'H2' denotes the higher hairpin. (b) Instantaneous flow field in the streamwise-wall normal plane. The gray contour indicates λ_{ci} value. The blue dashed line refers to the zero streamwise fluctuation velocity. The black solid line indicates the inclination angle of the envelope of hairpins.

The side view of the hairpin packet in Fig. 2(a), indicated by the solid black frame and green letters 'Plane I', is shown in Fig. 2(b) for a closer observation. The contour is the λ_{ci} value multiplied by the sign of the spanwise vorticity ω_z, i.e., $\mathrm{sgn}(\omega_z) \cdot \lambda_{ci}$. After subtracting $0.8U_e$, the heads of hairpins show the patterns of swirling motion. As hairpins travel downstream, their cross sections become larger but their vorticities are weaker due to the vorticity conservation law. This can be seen from the comparison between the swirling strengths of the hairpin heads. These two hairpins align in the streamwise direction separating about 0.5δ and their continuous induction creates a long-extended correlated uniform low-momentum zone denoted by the blue dashed line in Fig. 2(b). The envelope of heads of the hairpins creates an inclination of 14° with respect to the streamwise direction, marked by the black solid line in Fig. 2(b). The inclination angle is in a range of 9°–15° reported by Adrian *et al.*[10] The upstream hairpin induces the high-speed motion over its head which sweeps downwards and downstream and meets the upward ejection motion induced by the downstream hairpin, resulting in a cancelation between the two different induced motions. The influences of the low-speed and high-speed fluid create an identifiable shear layer. Within the shear layer there exists a point called 'stagnation point' at which the two opposite inductions nearly cancel each other. Beside these kinetic descriptions, the following conditionally-averaged analyses reveal the dynamic role in turbulent boundary layer.

3.2. Conditionally-averaged coherent structure

Figure 3(a) shows the conditionally-averaged coherent structure in the streamwise-wall normal plane. The detection event is $\lambda_{ci} < -10\bar{\lambda}_{ci}$ and λ_{ci} is the local minimum at $y^+ = 203$. λ_{ci} is multiplied by the sign of the spanwise vorticity so as to distinguish the direction of swirling motions and $\bar{\lambda}_{ci}$ is the mean absolute value of λ_{ci}. The combined conditions result in the extraction of strong swirling motion in the spanwise detection. The velocity vector pattern is consistent with the side-view signatures of hairpins proposed by Tomkins and Adrian.[11] A spanwise swirling motion located at the detected point represents the hairpin head. The ejected fluid moves upstream and meets with the sweep fluid which moves downstream. A shear layer pointed in Fig. 3(a) forms along the interface of the impact between the decelerated and accelerated fluids. The inclination angle of the shear layer is 52°, which is smaller than the instantaneous inclination angle like in Fig. 2(a) but represents the mean inclination angle of hairpins. The inclination of hairpins is important for the production of energy-containing events. The ejection event, the sweep event,[32,33] and the impact between them is crucial to the transport of the turbulent energy,[34,35] furthermore to the production and self-sustaining of turbulence.

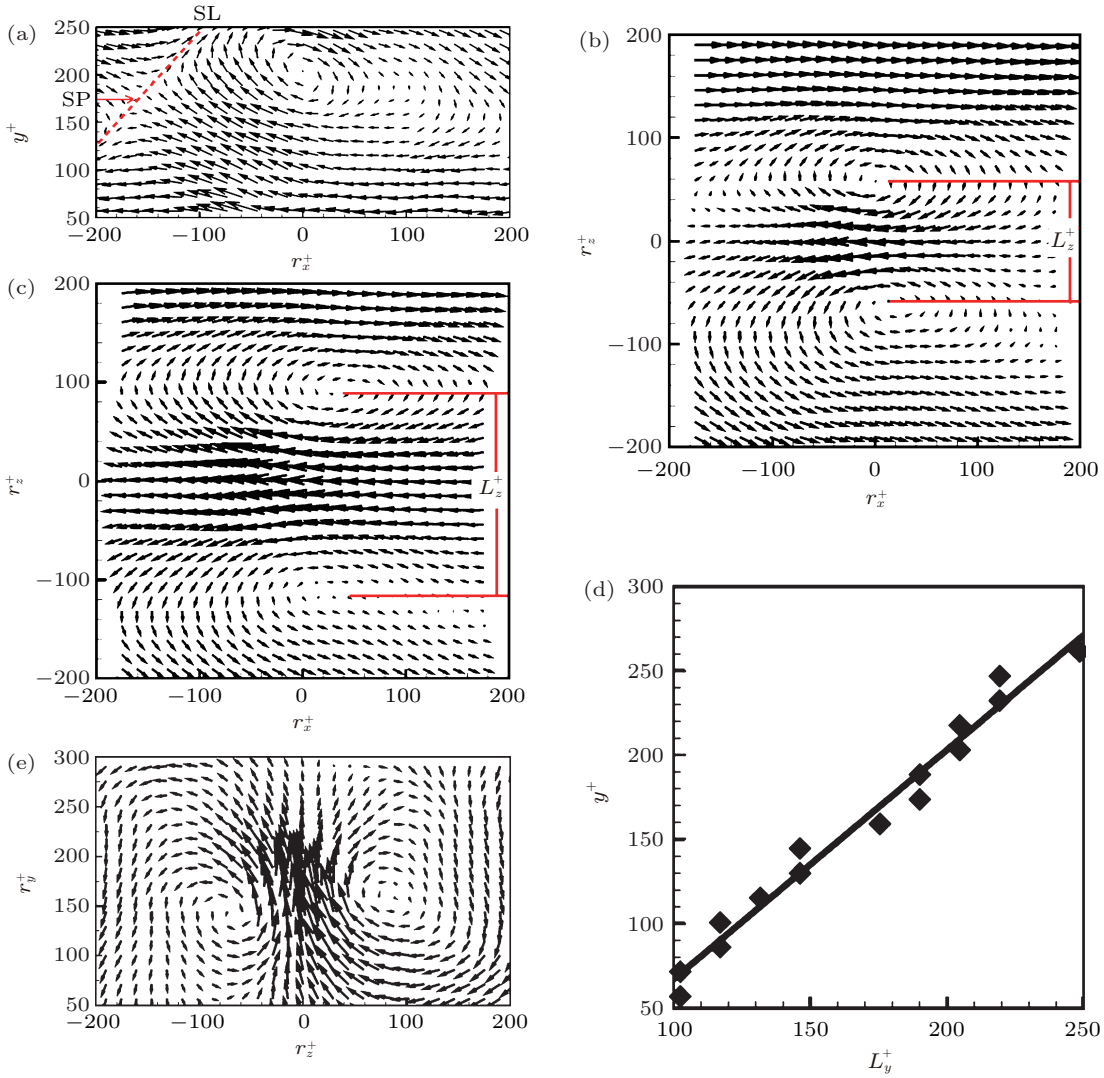

Fig. 3. (color online) (a) Conditionally-averaged structure in the streamwise-wall normal plane. The shear layer ('SL') is indicated by the red dashed line. 'SP' refers to the stagnation point. (b) Conditionally-averaged structure in the streamwise-spanwise plane with $k_2 = 0.8$. The red solid line indicates the spanwise separation of the cores of the swirling motions. (c) Conditionally-averaged structure in the streamwise-spanwise plane with $k_2 = 0.75$. (d) Spanwise scale of the pair of swirling motions versus y^+. (e) Conditionally-averaged structure in the wall normal-spanwise plane.

The conditionally-averaged coherent structures in the streamwise-spanwise plane are shown in Figs. 3(b)–3(d). The detection event takes place when $u < k_2 U_e$ and u is local minimum. The condition captures coherent structures which make the strong back-induction.[36] A low-momentum zone around the detected point is flanked by a pair of swirling motions. Figures 3(b) and 3(c) display the results with different values of threshold value k_2, 0.8 and 0.75 respectively at $y^+ = 203$. The larger value of k_2 means that more samples are included, meanwhile the smaller value of k_2 means that comparatively strong back-induction samples are included. It is indicated that the stronger back-induction is connected to the more mature or larger legs of hairpins which have larger diameter and area of induction. The streamwise and spanwise ranges of low-momentum zones both increase under larger swirling motions. The separation between the swirling cores is defined as the spanwise scale "L_z^+". In 'attached eddy hypothesis',[37] the scale of hairpins should be proportional to the wall-normal distance from the wall. Figure 3(d) confirms the scaling relationship or growth rate of hairpins. The linearly fitted growth rate is 0.74 in the present case and close to 0.9 given by Tomkins and Adrian.[11]

The conditional-averaged structure in the wall-normal-spanwise plane is shown in Fig. 3(e). The detected event is the event that takes place when $v > 0$ and v is local maximum. The simple detection condition reveals the most probable coherent structure that is responsible for the upward wall-normal motion. The result presents a region of upward motion flanked by a pair of anti-symmetric swirling motions.

By virtue of 3D PIV, we can comprehensively extract the characteristics of the coherent structures from different views and thus understand their role in the dynamic of turbulence, for example, they are responsible not only for the ejection and sweep events but also for the turbulent energy transport, such as the streamwise turbulent energy is delivered to the wall-normal and spanwise ones.

4. Space–time correlation

Correlations[24,25,38,39] are always useful tools for analyzing the coherent structures because they provide statistical information about the micro- and macro-scales. In the present paper the space–time correlation is defined as

$$C(r,\tau;y)=\frac{\overline{u'(x,y,z,t)u'(x+r,y,z,t+\tau)}}{u'_{\rm rms}(x)u'_{\rm rms}(x+r)}, \tag{4}$$

where u' is the streamwise fluctuation velocity, $u'_{\rm rms}$ is the rms of the streamwise fluctuation velocity. In Eq. (4), the ensemble is implemented in streamwise, spanwise direction, and time. Figures 4(a) and 4(b) show the surface and contour of the space–time correlation at $y^+=56.8$. τ^+ is the normalized time delay and r^+ is the normalized space separation. The correlation coefficient C is in a range from 0.5 to 0.9 in steps of 0.05. From Fig. 4, it is obvious that the correlation function has an elliptic shape which is predicted in the elliptic model. There are two recognizable characteristics for these elliptic iso-correlation curves: One is that the entire iso-correlation curves share a uniform preferred orientation whose slope is mainly determined by the convection velocity $U_{\rm c}$, and the other is that each of all the iso-correlation curves has a constant aspect ratio which can be derived from the Kolmogorov similar hypothesis. In Taylor hypothesis when the space separation becomes large, the correlations remain unchanged. Such a behavior violates the principle that correlations should decay with increasing the separation. Instead the elliptic model correctly captures the de-correlation process in the flow. More detailed results of space–time correlations and validations of the elliptic model can be found in our paper.[40]

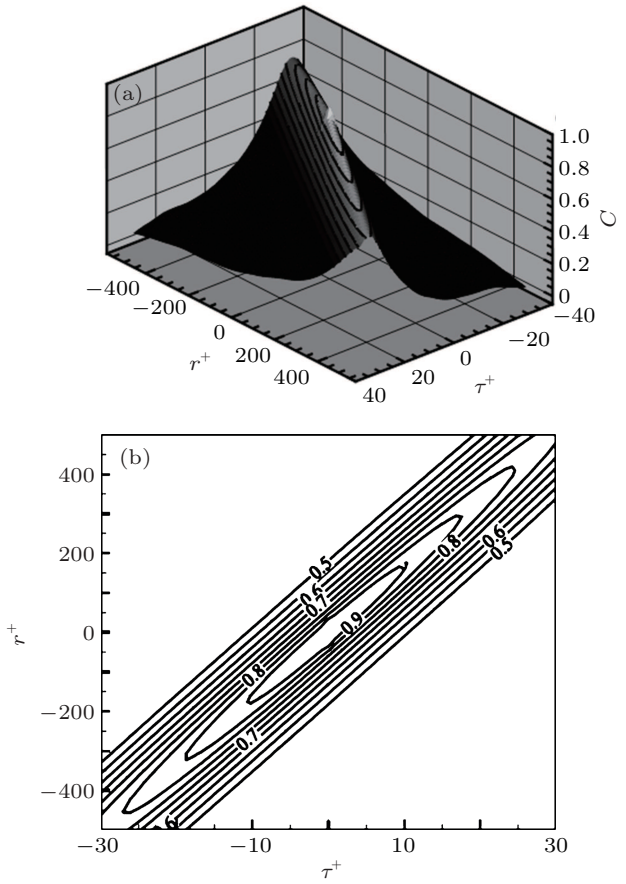

Fig. 4. (a) Surface and (b) contour of the space–time correlation at $y^+=56.8$.

5. Convection of coherent structures

5.1. Convection velocity from space–time correlation and conditional-averaged results

The convection of coherent structures in turbulent flow is an important phenomenon and issue for turbulence. Several schemes[41–44] have been proposed to define the convection velocity. We determine the convection velocity $U_{\rm c}$ based on

$$\left.\frac{\partial r_{\rm E}}{\partial r}\right|_{\tau}=0 \text{ and } r^*=U_{\rm c}\tau, \tag{5}$$

where r^* maximizes the correlation coefficient C for a given τ. The convection velocity $U_{\rm c}$ is estimated by linearly fitting the slope of $r^*(\tau)$, referring to as 'linear fit $U_{\rm c}$'. The estimated convection velocity is plotted by solid black squares in Fig. 5. The solid line in the plot represents the mean velocity. Another convection velocity calculated by the conditional-averaged method is presented by empty diamonds. The method first extracts vortices whose $\lambda_{\rm ci}$ exceeds $8\bar{\lambda}_{\rm ci}$ and is a local maximum, and then averages the streamwise velocity of the detected vortices. The convection velocity changes from $0.68U_{\rm e}$ to $0.85U_{\rm e}$, which accords with the range of Adrian *et al.*'s results.[10] In their work, the old larger hairpin packets move at $0.8U_{\rm e}$–$0.9U_{\rm e}$, occupying higher location meanwhile the young smaller hairpin packets move at $0.6U_{\rm e}$–$0.7U_{\rm e}$ occupying lower location. It is found that the convection motions gradually reach the mean velocity away from the wall, which is similar to the tendency shown in Pan *et al.*'s work.[45] Alamo and Jiménez[27] proposed an approximate formula in which the convection velocity is regarded as the average of the mean velocity profile with

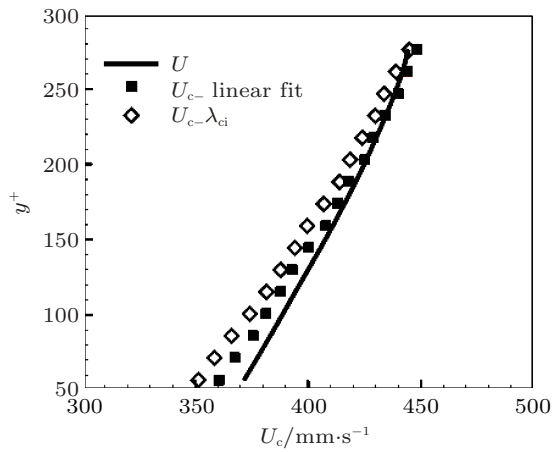

Fig. 5. Distributions of the convection velocity $U_{\rm c}$ along the wall-normal direction.

a weight function. Because the conditional-averaged convection velocity is calculated based on the real swirling motions in the flow, it has more realistic significance than the convection velocity calculated from the correlation. The detection condition collects strong swirling motions but excludes some coherent motions like low-momentum zones.

5.2. Fourier decomposition results

Taylor hypothesis assumes that the convection velocity is independent of scale and simply equal to the local mean velocity. But in reality the large- and small-scale coherent motions have complicated interactions and move at different velocities. For determining the convection velocities of different scales of coherent motions, the fluctuation velocity fields are decomposed by fast Fourier transform (FFT) in the streamwise and spanwise direction respectively. Every individual Fourier mode is reconstructed into a flow field from which the space–time correlation is calculated. Then a convection velocity for each scale is estimated based on Eq. (5). Figure 6 shows the relationships between the convection velocity and the Fourier modes in the streamwise and spanwise direction respectively at $y^+ = 56.8$, 130, and 203. It is demonstrated that the convection velocity has marginal dependence on the streamwise scale across the logarithmic layer. Despite the jitter induced by the limited resolution and measurement uncertainty, the convection velocities of different streamwise scales are around their own constant values which are regarded as the mean values and indicated by three lines in the plot. Although the convection velocities of the first 7 modes are larger than those of the latter 5 modes, the dependence on streamwise scale is weak in a certain streamwise wavenumber range. The mean convection velocities at 3 heights are in accordance with the results in previous section. The present results are consistent with the numerical results obtained by Kim and Hussain,[25] but between them exists a slight difference, i.e., what they derived is the convection velocities of the equispaced band of streamwise wavenumber while what is calculated in the present paper is individual streamwise wavenumber.

Figure 6(b) displays the curves of convection velocity as a function of spanwise scale. Contrary to the streamwise scale, the convection velocity has a dramatic decrease with increasing the spanwise scale at $y^+ = 56.8$, but away from the wall the prominent dependence on the spanwise scale vanishes. The dependence on the spanwise scales is also observed in Kim's channel flow. In their channel flow, the convection velocity did not change with the spanwise wavenumber beyond $y^+ = 50$. Because the present flow has a larger Re than their limited Re, the wall-normal location where the flow is not sensitive to the spanwise scale lifts up. From the different behaviors of the dependence on the streamwise and spanwise scale it follows that the turbulent boundary layer is a complicated anisotropic flow field.

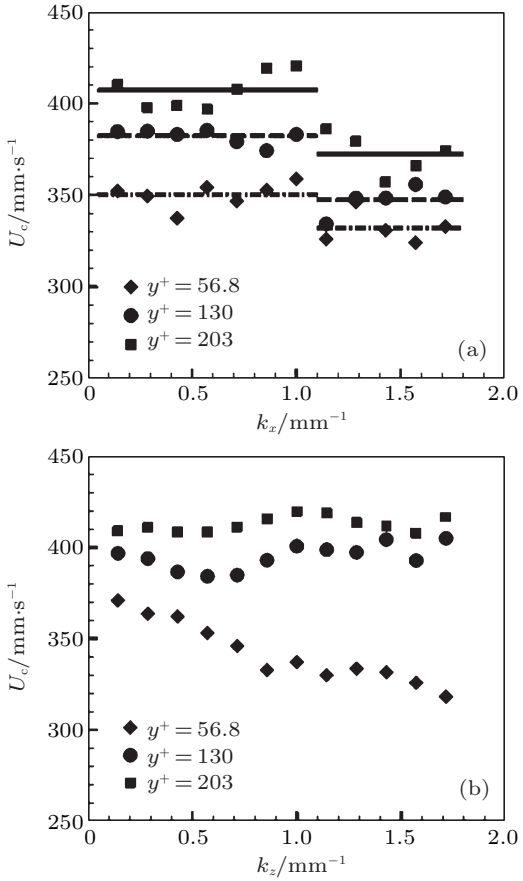

Fig. 6. Convection velocities with respect to the (a) streamwise wavenumber and (b) spanwise wavenumber at $y^+ = 56.8$, 130, and 203.

5.3. Proper orthogonal decomposition results

Due to the mathematic property of the Fourier basis functions, Fourier decomposition (FD) has some inevitable limits like forced periodicity on the velocity signal and fixed basis functions. A new method called 'proper orthogonal decomposition (POD)'[46,47] is introduced into the analysis of turbulence. The POD is more physical because its basis functions are dependent on the flow field. In POD the fluctuation velocity field is approximately linearly expressed as

$$u'(\boldsymbol{x}) = \sum_k a_k(t)\varphi_k(\boldsymbol{x}), \tag{6}$$

where $\varphi_k(\boldsymbol{x})$ is the k-rank basis function, $a_k(t)$ is the corresponding k-rank time coefficient. The orthogonal basis functions $\{\boldsymbol{\varphi}(\boldsymbol{x})\}$ satisfy[46,47]

$$\int_\Omega \langle u'(\boldsymbol{x})u'(\boldsymbol{x}')\rangle \boldsymbol{\varphi}(x')\,\mathrm{d}x' = \lambda\boldsymbol{\varphi}(x), \tag{7}$$

where $C(\boldsymbol{x},\boldsymbol{x}') = \langle u'(\boldsymbol{x})u'(\boldsymbol{x}')\rangle$ is the 2-order space correlation. It is equally to solve the eigenvalue equation discretely

$$C(\boldsymbol{x},\boldsymbol{x}')\varphi_k(x) = \lambda_k\varphi_k(x), \tag{8}$$

λ_k is the eigenvalue corresponding to the k-rank eigenvector and indicates the relative turbulent kinetic energy of the k-order POD mode. The primary advantage of POD is that

it searches the optimal basis functions in energy-containing sense and thereby becomes powerful enough to analyze the kinetic and dynamic events in turbulence. POD has been successfully employed to extract the coherent structures in various turbulent flows.[48–52]

In the present case 308 snapshots of fluctuation velocity field are utilized for POD analysis. Figure 7(a) presents the POD spectra at $y^+ = 56.8$, 130, and 203. POD spectra contain information about turbulent eddies in a similar way to Fourier spectral analysis. While in FD the velocity field is regarded as the superstition of waves, the POD modes are closer to the properties of turbulent eddies. Because the rank of POD modes is based on the contribution to the turbulent kinetic energy, the 1st POD mode always has the most energy values that are 23.4%, 36.3%, and 35.5% respectively at $y^+ = 56.8$, 130, and 203. The large-scale coherent motion becomes more significant while the small-scale coherent motion has a decreasing contribution with increasing the height. It is consistent with the observation that the scales of coherent motions increase when moving away from the wall, in the instantaneous and conditionally-averaged flow field. At two higher locations, the spectra of POD almost overlap with each other, especially at small scales. It implies the existence of the similarity in the outer layer. Liu *et al.*[52] compared their POD spectra of channel flow with those of a boundary flow presented by Lu and Smith[53] and found a good correlation between them. This suggests that outer layer similarity exists at least in two types of wall-bounded turbulences. Figure 7(b) shows the cumulative energy contribution of POD modes to the total turbulent kinetic energy, and it is expressed as $\eta = \sum_1^k \lambda_i / \sum_1^n \lambda_j$. It is obvious that at higher location less POD modes are needed to reach the same energy level as at lower location. The numbers of POD modes at different turbulent kinetic energy levels are listed in Table 2.

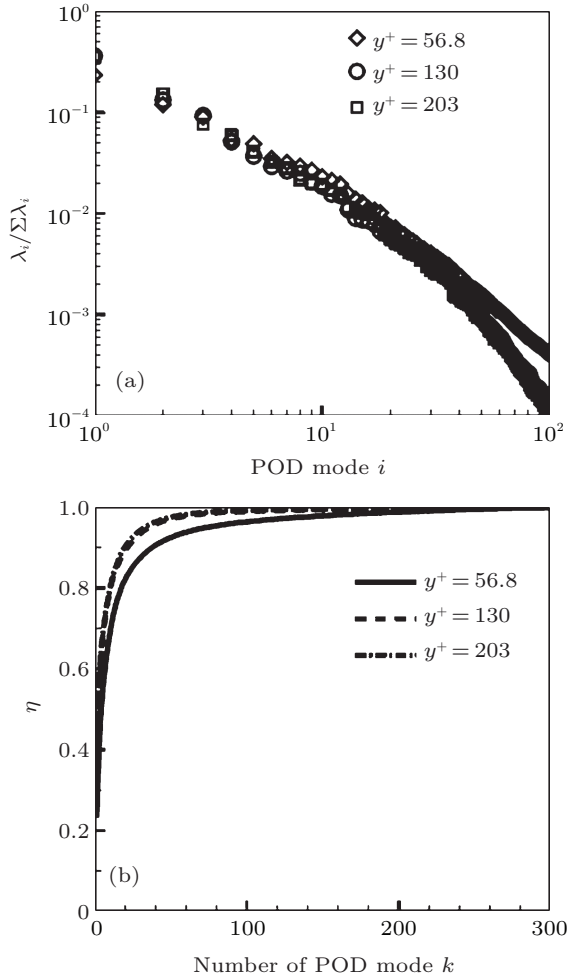

Fig. 7. (a) Spectra and (b) cumulative energy contributions of POD mode at $y^+ = 56.8$, 130, and 203.

Table 2. Numbers of POD modes for different values of η.

η/%	$y^+ = 56.8$	$y^+ = 130$	$y^+ = 203$
60%	7	3	3
65%	8	4	4
70%	10	6	6
75%	13	8	8
80%	18	10	10
85%	25	14	13
90%	38	22	19
95%	74	36	33

After decomposing the fluctuation velocity field into various scales of coherent motions, it is convenient to project the fluctuation velocity field onto POD modes. Authors use the first few low-order POD modes to reconstruct the large-scale velocity field which is equal to a low-pass filtered field. The velocity field composed of the residual high-order POD modes is regarded as the small-scale velocity field. These reconstructions involve some subjectiveness because it is hard to determine an unambiguous boundary to separate the large and small scales. Here the reconstructions of velocity fields are mainly based on η values in a range from 0.55 to 0.95. For brevity, the present work only shows two of the reconstructed velocity fields in the streamwise-spanwise plane at $y^+ = 56.8$ with $\eta = 0.65$ and 0.8. For the clarity of the visualization, only the local reconstructed velocity fields are displayed in Figs. 8(a)–8(c). The contours indicate the magnitudes of streamwise fluctuation velocities. The flow is from bottom to the top as indicated by the arrow. The reconstructed flow field in Fig. 8(a) has a low-speed zone between 0.2δ and 0.6δ in the spanwise direction. The dominant low-speed zone exceeds the streamwise range of the plot-1.25δ. It is noticed that even the velocity field has 65% of turbulent kinetic energy, there exist some important vortices pointed by circles and flanked by the low-momentum zones. A swirling motion at $z \approx 0.4\delta$ is between two large swirling motions. Two back-induced regions among the three vortices merge into a wide low-momentum zone. In Fig. 8(b) the additional small-scale

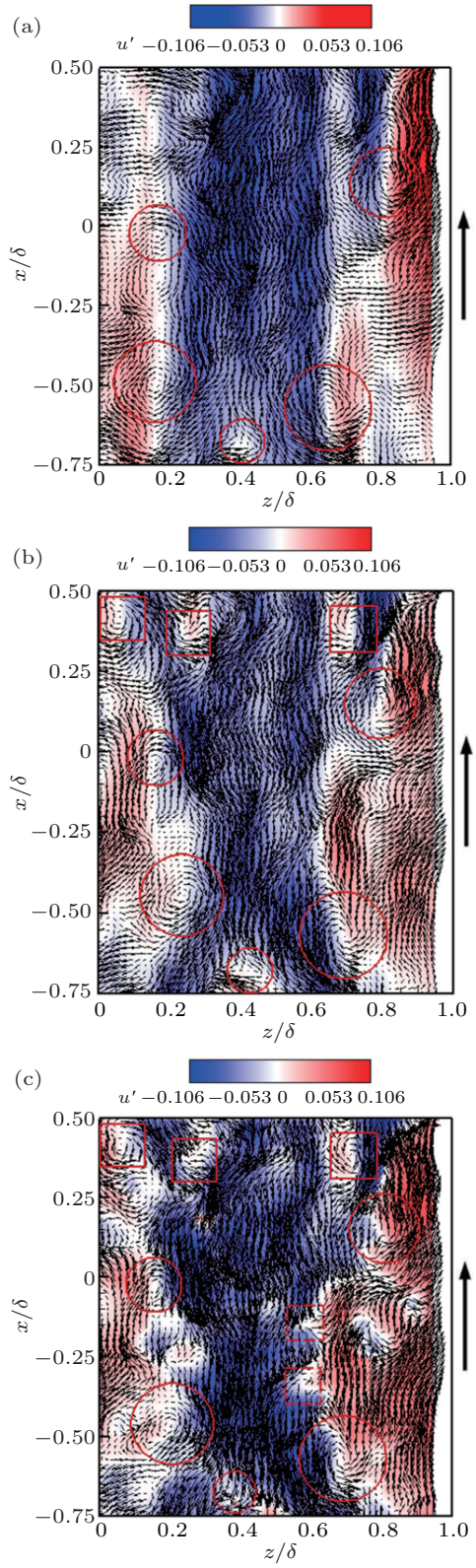

Fig. 8. (color online) Reconstructed velocity field with (a) $\eta = 0.65$, (b) $\eta = 0.8$, and (c) the original velocity field at $y^+ = 56.8$.

POD modes bring more fluctuations into the velocity field and three new swirling motions marked by squares appear. The new vortices align roughly in the spanwise direction at the downstream end of the low-momentum zone. The opposite induction effects appearing on their sides in the spanwise direction lead to the phenomenon that the high and low-speed zones are alternately distributed in the spanwise direction. The low-speed zone splits into several branches under the combined influence of multi-vortices. Besides the manipulation on the low-momentum zones, it is said that these coherent structures are responsible for the transport between the different components of turbulent kinetic energy, like those in the back-induction region just in the upstream of the merging region and the region in the middle of the downstream low-momentum zone where the streamwise component of energy turns into the spanwsie component. In Fig. 8(c), i.e., in the original velocity field, the fluctuation is too intensive to distinguish coherent interaction from the velocity field. The boundaries of low-speed zones are no longer smooth but the large-scale vortices identified before are still visible.

Although the marked vortices in Figs. 8(a)–8(c) are not the total swirling motions, they are good examples for demonstrating the significant events of dynamics. Plus, these scenarios confirm the model proposed by Elsinga[54] that large-scale structures, like vortices in Fig. 8(a), create and regulate the low-momentum zones and small-scale structures, like new vortices in Fig. 8(b), occur and evolve within or beside the low-momentum zones created by large-scale structures. POD method separates different scales of coherent motions and reveals the hierarchical relationships of various scales in turbulence dynamics.

After reconstructing the velocity fields of the large and small scales, their space–time correlations are calculated in terms of Eq. (4) and shown in Figs. 9(a) and 9(b). Both the space–time correlations of large- and small-scale velocity fields maintain the elliptic shape which implies that the elliptic model for the space–time correlation is still valid in the scale-separated reconstructed velocity fields. By contrast, the space–time correlations in two velocity fields have distinct characteristics. As expected from the previous large-scale instantaneous velocity fields which are mostly composed of large-scale uniform low-speed zones and accompanying vortices, the correlation of large-scale velocity field has a high correlated level. Meanwhile, the correlation of small-scale velocity field decays very fast from the center of correlation. The reconstructed small-scale velocity fields (not presented here) are filled with irregular distributed fluctuations and small-scale vortices. These vortices do not last in space nor in time and have poor correlativity. That they do not appear in the large-scale reconstructed velocity field implies that they do not play a critical role in the dynamical events of turbulence energy. It is noticed that on the sides of the positive correlation there are two negative correlation regions in the small-scale velocity field. It is explained that in the reconstructed small-scale velocity field the upstream motions and downstream motions alternately occur in the streamwise direction, which leads to the negative correlation in the plot.

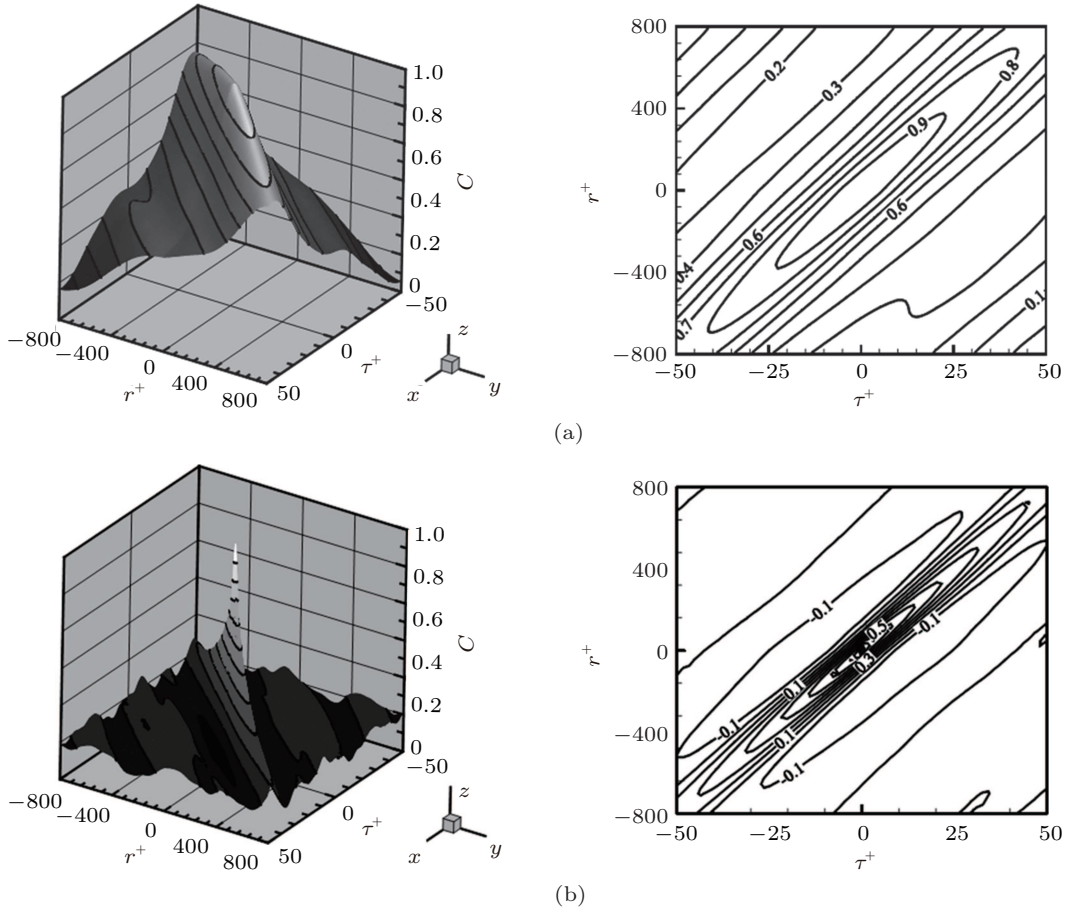

Fig. 9. Surfaces (left column) and contours (right column) of the space–time correlation in (a) large-scale velocity field and (b) small-scale velocity field at $y^+ = 56.8$.

Another parameter in the elliptic model is the sweep velocity V which follows

$$\left.\frac{\partial r_{\mathrm{E}}}{\partial \tau}\right|_r = 0 \ \text{ and } \ \tau^* = \frac{U_{\mathrm{c}}}{U_{\mathrm{c}}^2 + V^2} r, \tag{9}$$

where τ^* maximizes the correlation coefficient C for a given r. The results calculated from the large- and small-scale velocity fields are shown in Fig. 10(a). The solid symbols represent the large-scale velocity fields and the empty symbols denote the small-scale velocity fields. Squares refer to the convection velocity, and diamonds mean the sweep velocity. One solid line is added for indicating the convection velocity obtained from the original fluctuation velocity field. The dashed line represents the sweep velocity from the original fluctuation field. The relationship of convection velocity with scale and the relationship of sweep velocity with scale based on POD are distinctly different from the results obtained according to FD. The convection velocity of large-scale velocity field increases with the increase of energy ratio possessed by the field. It is surprising that the convection velocity of small-scale velocity field is roughly constant and higher than that of large-scale velocity field. The convection velocity of original velocity field is located in between the two velocities and is closer to that of small-scale velocity field. Due to the back-induction forced by vortices, the low-momentum zones which are dominant in large-scale velocity fields do not move fast. Combining with the conditionally-averaged convection velocity result of swirling motions in Subsection 4.1, it is speculated that the present result of large-scale velocity field mainly reveals the convection process of low-momentum zones. With the different convection velocities of large and small scales, it is explained that the missing swirling motions in the conditional detection in Subsection 4.1, which mainly exist in the small-scale velocity field, are responsible for the deficit of the conditionally-averaged convection velocity. In turbulence, small-scale eddies are carried by large-scale eddies, and during downstream movement the small-scale eddies experience intensive distortion under the influence of the large-scale eddies, decay fast and lead to a poor correlation level. In summary, the convection velocity of the original velocity field, i.e., the full-scale fluctuation velocity field is actually a mixture of the slow-moving large-scale and fast-moving small-scale coherent motions. The results of convection velocity based on POD method reveal a different scale-dependence from based on FD.

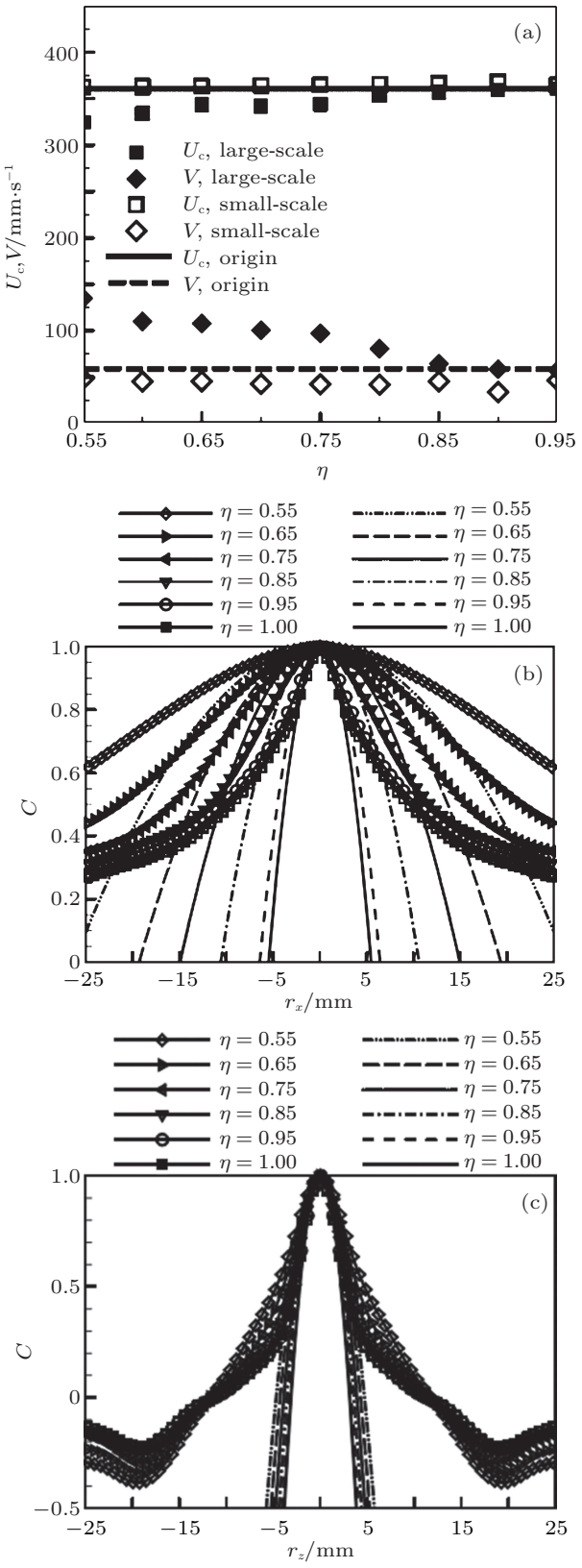

Fig. 10. (a) Convection velocity and sweep velocity of large- and small-scale velocity fields, and original fluctuation velocity field; (b) the streamwise correlation and (c) the spanwise correlation and corresponding osculating parabolas of large-scale velocity field.

It is found that with the η of large-scale velocity field increasing, the sweep velocity decreases. Meanwhile the sweep velocity of small-scale velocity field changes slightly. In He *et al.*'s theoretical analysis,[22] they concluded that the sweep velocity is associated with the mean shear S, the Taylor microscale λ, and the level of the fluctuation υ_0. All three statistical quantities are quadratically proportional to the sweep velocity. In the present work, although the turbulent boundary layer is more complicated than the homogeneous shear flow in their work, the relationships of factors with sweep velocity are valid. The mean shears of those reconstructed large-scale velocity fields are not expected to differ from each other very much. And with higher η, the turbulent kinetic energy increases, which leads to the increase of sweep velocity, but conversely, the decrease of sweep velocity. So it is speculated that the Taylor microscale plays a key role in sweep velocity. To try to understand the variation of sweep velocity with scale, we present the streamwise and spanwise correlations from $\eta = 0.55$ to 0.95, respectively in Figs. 10(b) and 10(c). In Ref. [55], the Taylor microscale is associated with the spatial correlation as

$$C = 1 - \frac{1}{2}\left(\frac{r}{\lambda}\right)^2 + \cdots, \tag{10}$$

where λ is the Taylor microscale. After determining the osculating parabola of the spatial correlation, the intercept of the osculating parabola on the abscissa will be $\sqrt{2}\lambda$. The obtained osculating parabolas are plotted in Figs. 10(b) and 10(c) as lines marked with no symbols. It is seen that from $\eta = 0.55$ to 0.95, the streamwise correlations decline and reach the correlated level of the original fluctuation velocity field, and the intercepts of the corresponding osculating parabolas become smaller. The spanwise correlations and Taylor microscale have the same tendency but are not so prominent as the streamwise ones. The reduction of the Taylor microscale with POD scale increasing is consistent with the reduction of sweep velocity with POD scale increasing. As for the influence of the Taylor microscale in small-scale velocity field, the spatial correlation decays fast and the reduction of the Taylor microscale is not so dominant as in large-scale velocity field, with which the constant distribution of sweep velocity can be explained.

6. Conclusions

A full-component velocity field of turbulent boundary layer is acquired using tomographic PIV to investigate the elliptic model for space–time correlation. Dominant coherent structures such as hairpin vortices, hairpin packets, and elongated low-momentum zones are visualized and their roles in the dynamics of turbulence are emphasized. The new elliptic model is validated through space–time correlations of the flow and is successful in the advancement of Taylor frozen hypothesis. Further investigation of parameters in the model gives the conclusions below.

(i) The convection velocity is scaled with the local mean velocity in the logarithmic layer of turbulent flow.

(ii) Stronger dependency on spanwise-scale is shown than on streamwise-scale for the convection velocity in near-wall region. It is explained that large-scale motions are more possible to relate with coherent structures away from the wall which move faster.

(iii) Through POD extractions of the energy-containing coherent motions in the flow, it is demonstrated that large-scale coherent structures induce the low-momentum zones where small-scale coherent structures reside.

(iv) Different distributions of the convection velocities of different scales are revealed from FD and POD analyses. It is seen that the large POD scale of coherent motion mainly represents the low-momentum zone, whilst the small POD scale represents low-correlated individual vortice. It is indicated that the sweep velocity is strongly associated with the fluctuation scale in the flow.

Acknowledgment

The authors sincerely thank all the members of the experimental team in TU Delft, LaVision GmbH, and the German Aerospace Center (DLR) for providing the Tomographic PIV data.

References

[1] Robinson S K 1991 *Ann. Rev. Fluid Mech.* **23** 601
[2] Kline S J, Reynolds W C, Schraub F A and Runstadler P W 1967 *J. Fuid Mech.* **30** 741
[3] Brooke J W and Hanratty T J 1993 *Phys. Fluids A* **5** 1011
[4] Jeong J, Hussain F, Schoppa W and Kim J 1997 *J. Fluid Mech.* **332** 185
[5] Schoppa W and Hussain F 2002 *J. Fluid Mech.* **453** 57
[6] Head M R and Bandyopadhyay P J 1987 *Fluid Mech.* **107** 297
[7] Adrian R J 1991 *Ann. Rev. Fluid Mech.* **23** 261
[8] Adrian R J 2005 *Exp. Fluids* **39** 159
[9] Elsinga G E, Scarano F, Wieneke B and van Oudheusden B W 2006 *Exp. Fluids* **41** 933
[10] Adrian R J, Meinhart C D and Tomkins C D 2000 *J. Fluid Mech.* **422** 1
[11] Tomkins C D and Adrian R J 2003 *J. Fluid Mech.* **490** 37
[12] Zhou J, Adrian R J, Balachandar S and Kendall T M 1999 *J. Fluid Mech.* **387** 353
[13] Stanislas M, Perret L and Foucaut J M 2008 *J. Fluid Mech.* **602** 327
[14] Schlatter P, Li Q, Brethouwer G, Johansson A V and Henningson D S 2010 *Int. J. Heat Fluid Flow* **3** 251
[15] Schröder A, Geisler R, Staack K, Elsinga G E, Scarano F, Wieneke B, Henning A, Poelma C and Westerweel J 2011 *Exp. Fluids* **50** 1071
[16] Panton R L 2001 *Progress in Aerospace Sciences* **37** 341
[17] Marusic I, McKeon B J, Monkewitz P A, Nagib H M, Smits A J and Sreenivasan K R 2010 *Phys. Fluids* **22** 065103
[18] Willmarth W W and Lu S S 1972 *J. Fluid Mech.* **55** 65
[19] Taylor G I1938 *Proc. R. Soc. Lond.* **164** 476
[20] Burghelea T, Segre E and Steinberg V 2005 *Phys. Fluids* **17** 103101
[21] He G W and Zhang J B 2006 *Phys. Rev. E* **73** 055303
[22] Zhao X and He G W 2009 *Phys. Rev. E* **79** 046316
[23] Guo L, Li D, Zhang X and He G W 2012 *Acta Mech. Sin.* **28** 993
[24] Zhou Q, Li C M, Lu Z M and Liu Y L 2011 *J. Fluid Mech.* **683** 94
[25] Kim J and Hussain F 1992 *Phys. Fluids* **5** 695
[26] Krogstad P, Kaspersen J H and Rimestad S 1997 *Phys. Fluids* **10** 949
[27] Del Alamo J C and Jiménez J 2009 *J. Fluid Mech.* **640** 5
[28] Elsinga G E, Poelma C, Schröder A, Geisler R, Scarano F and Westerweel J 2012 *J. Fluid Mech.* **697** 273
[29] Jeong J and Hussain F 1995 *J. Fluid Mech.* **285** 69
[30] Chakraborty P, Balachandar S and Adrian R J 2005 *J. Fluid Mech.* **535** 189
[31] Liu X B, Chen Z Q and Liu C Q 2010 *Chin. Phys. Lett.* **27** 024706
[32] Liu J H and Jiang N 2007 *Chin. Phys. Lett.* **24** 2617
[33] Lian Q X and Guo H 2004 *Acta Phys. Sin.* **53** 2226 (in Chinese)
[34] Johansson A, Alfredsson P H and Kim J 1991 *J. Fluid Mech.* **224** 579
[35] Jiang N, Guan X L, Yang S Q and Yao S Y 2012 *Proceedings of* 7*th National Conference on Fluid* Mechanics, 2012, Guilin, China, p. 11
[36] Tang D B, Chen L and Liu C Q 2011 *Acta Phys. Sin.* **60** 094702 (in Chinese)
[37] Townsend A A 1976 *The Structure of Turbulent Shear Flow*, 2nd edn. (Cambridge: Cambridge University Press) pp. 272–94
[38] Ganapathisubramani B, Clemens N T and Dolling D S 2006 *J. Fluid Mech.* **556** 271
[39] Ganapathisubramani B 2007 *Phys. Fluids* **19** 098108
[40] Wang W, Guan X L and Jiang N 2014 *Acta Mech. Sin.* **30** 468
[41] Moin P 2009 *J. Fluid Mech.* **640** 1
[42] Wills J A B 1964 *J. Fluid Mech.* **20** 417
[43] Hussain A and Clark A R 1981 *AIAA Journal* **19** 51
[44] Goldschmidt V W, Young M F and Ott E S 1981 *J. Fluid Mech.* **105** 327
[45] Pan C, Wang J J and Zhang C 2009 *Sci. China Ser. G: Phys. Mech. Astron.* **52** 248
[46] Berkooz G, Holmes P and Lumley J L 1993 *Ann. Rev. Fluid Mech.* **25** 539
[47] Chatterjee A 2000 *Current Science* **78** 808
[48] He J and Fu S 2003 *Acta Mech. Sin.* **35** 385
[49] Pan C, Wang H and Wang J J 2013 *Measurement Science and Technology* **24** 055305
[50] Sirovich L, Kirby M and Winter M 1990 *Phys. Fluids A: Fluid Dynamics* **2** 127
[51] Prabhu R D, Collis S S and Chang Y 2001 *Phys. Fluids* **13** 520
[52] Liu Z, Adrian R J and Hanratty T J 2001 *J. Fluid Mech.* **448** 53
[53] Lu L J and Smith C R 1991 *Exp. Fluids* **11** 247
[54] Elsinga G E 2008 "Tomographic Particle Image Velocimetry" (Ph. D. Thesis) (Delft: Technology University of Delft)
[55] Shi X G 1994 *Turbulence* (Tianjin: Tianjin University Press) pp. 50–52 (in Chinese)